Biosensors and Bioelectronics 287 (2025) 117677

Contents lists available at ScienceDirect

Biosensors and Bioelectronics

journal homepage: www.elsevier.com/locate/bios

Nanostructure-gated organic electrochemical transistors for accurate glucose monitoring in dynamic biological pH conditions

Ke Meng [a], Jia Zhu [a,b,*], Tianyao Zhang [a], Xianzhe Zhang [c], Yingying Zhang [d], Xiangjie Chen [a], Fan Li [a], Yao Tong [d], Senhao Zhang [d], Donghai Qiu [d], Hongbo Yang [d], Shangbin Liu [e], Lan Yin [e], Rui Zhao [f], Libin Huang [f], Tao Li [f], Min Gao [a], Taisong Pan [a], Jian Yang [g], Huanyu Cheng [c,**], Yuan Lin [a,h,***]

[a] School of Materials and Energy, University of Electronic Science and Technology of China, Chengdu, 610054, China
[b] Yangtze Delta Region Institute (Quzhou), University of Electronics Science and Technology of China, Quzhou, 324000, China
[c] Department of Engineering Science and Mechanics, The Pennsylvania State University, University Park, PA, 16802, USA
[d] Suzhou Institute of Biomedical Engineering and Technology, Chinese Academy of Science, Suzhou, 215011, China
[e] School of Materials Science and Engineering, Tsinghua University, Beijing, 100084, China
[f] Department of Gastroenterology, West China Hospital, Sichuan University, Chengdu, 610041, China
[g] Research Center for Industries of the Future, Biomedical Engineering Program, School of Engineering, Westlake University, Hangzhou, Zhejiang, 310030, China
[h] Medico-Engineering Cooperation on Applied Medicine Research Center, University of Electronics Science and Technology of China, Chengdu, 610054, China

ARTICLE INFO

Keywords:
Non-enzymatic glucose sensor
Organic electrochemical transistor
Laser-induced graphene nanocomposite
Self-pH calibration
Long-term stability

ABSTRACT

Non-invasive, real-time, and continuous monitoring of trace amounts of glucose in near-neutral biofluids is significant for the daily care and treatment of diabetic patients or people with suboptimal health status. Despite improved sensing performance with novel low-dimensional materials or porous structures in various enzymatic and non-enzymatic electrochemical glucose sensors, they still suffer from high cost, poor long-term stability, and performance fluctuations in varied temperature and pH. This work synergistically combines an Au-modified porous laser-induced graphene (LIG) gate electrode with an organic electrochemical transistor (OECT) to create a flexible non-enzymatic glucose sensor. The resulting OECT-based non-enzymatic glucose sensor exhibits significantly enhanced sensitivity in near-neutral biofluids, the limit of detection (LOD) (0.08 μM in pH = 7.4), excellent stability over time (degradation of ~10 % in 180 days) and against temperature changes (30 °C–40 °C), self-pH calibration capabilities, and uncompromised sensing performance with shrinking sizes. The highly consistent laser patterning technique and *in situ* galvanic reduction process for electrode modifications not only provide a simple yet versatile approach to creating low-cost, compact sensing platforms for precise and real-time sweat glucose measurements but also support scalable production, allowing the correlation study of key biomarkers in sweat and blood.

1. Introduction

Continuously quantifying the glucose concentration in different biofluids has great clinical implications for the evaluation of chronic diseases and metabolic processes. Despite the existence of the gold standard measurements with isotope dilution gas chromatography-mass spectrometry, continuous and real-time monitoring of glucose concentration with precision meeting clinical requirements remains a formidable challenge in both health management and chronic disease treatments (Volmer et al., 2015; Rodríguez-González et al., 2005). Efforts to tackle this challenge have led to the innovation of various optical or electrochemical sensors in wearable form. Depending on the working wavelength, the optical sensor that leverages the interaction between light and the glucose molecule can be categorized into near-infrared (NIR), mid-infrared (MIR), Raman, and photoacoustic (PA) spectroscopy (Ahmed et al., 2022; Yu et al., 2021). Since the glucose

* Corresponding author. School of Materials and Energy, University of Electronic Science and Technology of China, Chengdu, 610054, China.
** Corresponding author.
*** Corresponding author. School of Materials and Energy, University of Electronic Science and Technology of China, Chengdu, 610054, China.
E-mail addresses: zhujia1990@uestc.edu.cn (J. Zhu), huanyu.cheng@psu.edu (H. Cheng), linyuan@uestc.edu.cn (Y. Lin).

https://doi.org/10.1016/j.bios.2025.117677
Received 8 April 2025; Received in revised form 13 May 2025; Accepted 7 June 2025
Available online 7 June 2025

concentration is calibrated by the transmission or reflection strength, the optical sensor often involves the use of delicate, expensive, and bulky optical systems, which severely restricts its application in point-of-care settings. Electrochemical sensors featuring simple structures and low cost have been proposed to mitigate this issue (Handbook of Nanobioelectrochemistry, 2023; Kumar et al., 2019). The flexible/stretchable electronics with integrated electrochemical sensors in the form of bio-patches or microneedles allow non-invasive, real-time, and on-site measurements of the glucose concentration in biofluids, including saliva, tears, sweat, and tissue fluids (Bakhshandeh et al., 2024; Benedetti et al., 2024; Zhang et al., 2024; Zheng et al., 2024; Lorestani et al., 2023). It is feasible to infer the glucose concentration in the blood by exploiting the correlation between the blood glucose and that in the other biofluids (Reddy et al., 2022; Malik et al., 2016).

Despite significant advances, electrochemical glucose sensors still suffer from intrinsic limitations for mass production and commercialization, including poor sensitivity, stability, and repeatability (Hassan et al., 2021; Park et al., 2006; Farahmandpour et al., 2022). Based on the working principle, electrochemical glucose sensors are categorized into either enzymatic (based on glucose oxidases or glucose dehydrogenases) (Kim et al., 2022; Ferri et al., 2011; Baghayeri et al., 2017; Okuda--Shimazaki et al., 2020) or non-enzymatic (based on noble metals or transition metal oxides) (Thanh et al., 2016a; Hoa et al., 2015; Zhu et al., 2016; Madhu et al., 2015). The former demonstrates high specificity but suffers from poor long-term stability, and temperature/pH sensitivity, while the latter exhibits relatively good stability, excellent temperature immunity, and generally superior sensitivity compared to the former (Park et al., 2006; Govindaraj et al., 2023; Wilson and Turner, 1992). However, these non-enzymatic glucose sensors, which rely on traditional three-electrode configurations, typically require operation in strongly alkaline solutions (e.g., NaOH) and exhibit insufficient detection limits in near-neutral biological fluids, thereby limiting their applicability in wearable devices. Extensive efforts have been devoted to addressing this challenge. One strategy involves reducing alkaline dependency, for example, by developing NaOH/Nafion/PEO hybrid films that sustain a strongly alkaline microenvironment (local pH $>$ 10) in sweat through the gradual release of NaOH (Liang et al., 2024). Alternatively, microreaction chambers encapsulating small amounts of alkaline solution have been employed to introduce sweat for testing (Zhu et al., 2021a). Other approaches aim to enhance the sensitivity of non-enzymatic glucose sensors under neutral conditions, such as increasing the electrode's specific surface area using Pt-PLA nanoparticles or AMWCNTs/AuNPs composites (Han et al., 2020; Chen et al., 2024). However, their detection limits or linear detection ranges still fail to fully cover the glucose concentrations in human biofluids. Additionally, due to the potential drift of reference electrode in three-electrode configurations, non-enzymatic glucose sensors suffer from gradual performance degradation over time (Søpstad et al., 2018; Yang et al., 2009). Their sensitivity also significantly decreases with electrode size reduction, limiting the miniaturization and high-density integration of wearable devices (Karyakin et al., 2007; Siddiqui et al., 2010).

Recently, it has been reported that exploiting the transconductance of field effect transistors (FETs) (Kaisti, 2017; Rollo et al., 2020; Hangarter et al., 2010) or organic electrochemical transistors (OECTs) (Zhang et al., 2018; Sophocleous et al., 2021; Wu et al., 2024; Zhao et al., 2023) can significantly improve the limit of detection (LOD) of electrochemical sensors. These FET or OECT-based electrochemical glucose sensors are based on gated electrodes modified with recognition receptors (including enzymes, antibodies, and aptamers) for high specificity. Different from the conventional three-electrode configuration, the reaction at gate electrodes leads to a net flux of faradaic current at the gate/electrolyte interface, which alters the effective gate voltage and consequently the drain current with an amplification effect (Torricelli et al., 2021; Ghittorelli et al., 2018; Kergoat et al., 2012). Despite the enhanced sensitivity from the field effect, these field effect-based glucose sensors still suffer from complex enzyme immobilization steps and poor stability and performance fluctuations with changes in pH/temperature due to rapid receptor degradation (Sheldon and van Pelt, 2013; Valdes and Moussy, 2000).

This work introduces the first laser-fabricated flexible OECT-based non-enzymatic glucose sensor gated by a chemically modified laser-induced graphene (LIG) electrode with enhanced sensitivity, LOD, excellent long-term stability, and accurate measurements against the pH/temperature fluctuations in various biofluids. Porous LIG electrodes prepared and patterned by a low-cost and highly efficient laser scribing can be uniformly modified with Au nanocluster (AuNC) by a controllable and consistent *in situ* galvanic reduction process, exhibiting great potential in miniaturization and scalable production of flexible glucose sensors for extensive correlation studies. The pH-dependent conductivity of poly (3,4-ethylenedioxythiophene) polystyrene sulfonate (PEDOT:PSS) was further exploited to self-calibrate pH variations in biofluids for reduced interferences and improved accuracy. Impressively, different from electrochemical sensing in conventional three-electrode configurations, the OECT-based sensing mechanism ensures uncompromised glucose sensing performance with shrinking overall sizes by simply fixing the gate/channel ratio. The design and demonstration of the AuNC/LIG nanocomposite-gated OECT also provide a platform to further decorate aptamers and molecularly imprinted polymers for highly sensitive and stable detection of other biomarkers in different clinical applications.

2. Experimental section

2.1. Materials

Gold chloride trihydrate ($\geq$99.9 % trace metals basis) was purchased from Sigma-Aldrich. PEDOT:PSS was purchased from Xi'an Polymer Light Technology Co., Ltd. 3-Glycidyloxypropyltrimethoxysilane (97 %) and Dodecylbenzenesulfonic acid (90 %) were obtained from Shanghai Macklin Biochemical Co., Ltd. Ethylene glycol (98 %) was purchased from Beijing Dehang Wuzhou Technology Co., Ltd. Polyimide (PI) films (50 μm thick) were purchased from DuPont, USA. Polyethylene glycol terephthalate (PET) films (100 μm thick) were purchased from 3M. All chemicals were used without further purification.

2.2. Fabrication of OECT-based non-enzymatic glucose sensors

After rinsing with ethanol and ultrapure water, the PI film was attached to a glass substrate coated with a thin PDMS layer (100 μm) as the adhesive. A thin Ti/Au layer (5 nm/100 nm) was deposited on the PI film via magnetron sputtering, followed by a lift-off process to serve as the source and drain electrode of OECT. PEDOT:PSS precursor solutions were prepared by stir mixing 94 wt% PEDOT:PSS, 5 wt% ethylene glycol, 1 wt% GOPS, and 0.1 wt% DBSA for 1 h. The PEDOT:PSS precursor solution was spin-coated onto the PI film with a speed of 500 rpm for 6s and 2500 rpm for 30s, followed by annealing at 120 °C for 1 h to obtain a thin film of 200 nm. Ethylene glycol, GOPS, and DBSA were used to improve the conductivity and mechanical stability of the PEDOT:PSS film. The PEDOT:PSS thin film was patterned through photolithography and reactive ion etching (RIE, 90 mT pressure, 100 sccm O_2, 5 sccm SF_6, with 100 W for 240 s) to serve as the channel of OECT. The dimension of the channel in this work was set to 0.1 mm (L) $\times$ 2 mm (W), which also allows facile UV laser scribing. Photolithography and laser scribing processes were used for the fabrication of a single OECT unit and the array, respectively. A thin film of SU-8 3050 photoresist (~10 μm thick) was patterned to passivate the drain and source electrode while exposing the channel region.

The LIG electrode was prepared and patterned with one-step laser scribing (wavelength of 10.6 μm, spot size of 127 μm, and pulse duration of 17 μs). A CO_2 laser was employed in the raster mode with power of 10.5 % (equivalently power density of 24.8 kW/cm^2), scanning speed of 11 % (140 mm/s), PPI of 1000, and image density of 6 to create LIG

electrodes on the PI film. Next, the LIG electrode was uniformly modified with AuNC by *in situ* galvanic reduction. To be specific, the LIG electrode with an external copper foil connected by a thin silver wire was immersed in $HAuCl_4{\cdot}3H_2O$ solutions. After a 1-h reaction and rinsing with ultrapure water, the Nafion precursor was drop-cast on the AuNC/LIG electrode to complete the fabrication process. The galvanic reduction process can be applied to a LIG electrode array with high yield, efficiency, and consistency for scalable production.

2.3. Materials characterization of LIG and AuNC/LIG electrodes

Scanning electron microscope (SEM) and energy dispersive spectrometer (EDS) characterizations of different gate materials were obtained by a field emission scanning electron microscope (FESEM, JSM-7500 F, JEOL Ltd.). Raman spectroscopy was carried out using a Renishaw InVia Qontor Raman spectrometer at room temperature, with an excitation curve wavelength of 532 nm, a spectral range of 100–3000 cm^{-1}, and a spectral resolution of 0.5 cm^{-1}. X-ray diffraction (XRD) analysis was measured using the BRUKER D8 Advance XRD system (Cu-Kα radiation, $\lambda = 0.15418$ nm). X-ray photoelectron spectroscopy (XPS) spectra were obtained by a K-Alpha X-ray photoelectron spectrometer using Al Kα radiation (0.6 eV) (ESCALAB Xi+, Thermo Fisher Scientific Inc.).

2.4. Electrochemical characterization of LIG, p_Au, and AuNC/LIG electrodes

Electrochemical characterizations, including Cyclic Voltammetry (CV) and Electrochemical impedance spectroscopy (EIS) of different gate materials were measured using an electrochemical workstation (CHI760E, CH Instruments Inc.). A traditional three-electrode configuration was used for CV and EIS measurements with a commercial Ag/AgCl reference electrode and a platinum wire as the counter electrode. The obtained EIS data were fitted by the Zview software.

2.5. Electrical characterization and glucose-sensing performance of OECTs

Transfer characteristic of OECTs was measured with a semiconductor device parameter analyzer (Keysight B1500A) with V_{ds} fixed at −0.5 V and V_{gs} ranging from −0.4 V to 0.6 V. Sensing performance (i.e., the amperometric response) of the OECT-based non-enzymatic glucose sensor with the addition of glucose was measured by a dual-channel electrochemical workstation (CHI760E, CH Instruments Inc.). The interference test for the non-enzymatic OECT-based glucose sensor was conducted following well-accepted protocols (Chiu et al., 2020a; Xu et al., 2012; Lee et al., 2019; Bai et al., 2017; Chen et al.). The selection of interferents and their concentrations were based on the composition of the target biofluids, such as sweat in this study. The concentration of glucose, KCl, NaCl, sucrose, maltose, fructose, DA, AA, AP, and UA was set to 1 mM, and the concentration of 10 mM was used for lactose.

2.6. Preparation of the integrated wearable glucose sensors

After designing the microfluidic pattern with the CAD software, the PET film was patterned by laser scribing to create the inlet, microfluidic, and outlet layers (Won et al., 2013). The as-fabricated OECT-based non-enzymatic glucose sensor was sandwiched between the microfluidic and inlet layers. Next, a laser-patterned double-sided medical adhesive tape was laminated on the inlet layer to provide adhesion for the integrated device with human skin. A dual-channel miniaturized electrochemical workstation (BioSYS-P15E, Shenzhen Refresh Intelligent Technology Ltd.) with a built-in Bluetooth module was employed for real-time data sampling and wireless transmission to portable terminals (e.g., cellphones and tablets). All human subject studies were approved by the Institutional Review Board at Penn State University (#STUDY00020934).

3. Results and discussion

3.1. Design of the OECT-based non-enzymatic glucose sensor

Instead of measuring the oxidation current in the electrochemical glucose sensors with a conventional three-electrode configuration, the AuNC/LIG electrode in the PEDOT:PSS-based OECT serves as the gate electrode to significantly enhance the sensing performance by combining the transconductance and non-enzymatic sensing mechanism (Fig. 1). The detailed fabrication process of the OECT gated by the Au nanocluster (AuNC)-modified LIG electrode is depicted in the **Experimental section** and Fig. S1. Briefly, the AuNC/LIG was fabricated by first laser-scribing polyimide films to create LIG electrodes, then modifying them with AuNC via *in situ* galvanic reduction. The laser scribing, laser patterning, and galvanic reduction process can give a yield of thousands of samples per hour, which holds great potential for mass production (Fig. S2). The drain and source electrodes of the OECT can be fabricated by either conventional photolithography or low-cost and efficient laser engraving. A small channel length of ~15 μm can be easily obtained by laser engraving with high yield and consistency (Fig. S3). Considering its flexibility/programmability and compatibility with LIG preparation, laser engraving from a custom-built dual-laser system is explored to pattern the sensor array for mass production (Fig. S4).

3.2. Characterization of the AuNC/LIG electrode

SEM images show typical porous structures of the pristine LIG electrode with an average pore size of ~4 μm (Fig. 2a), which features a large surface area for electrochemical sensing and energy storage applications (Purohit et al., 2020). Raman spectroscopy of LIG exhibits three characteristic peaks: the D peak at 1340 cm^{-1}, the G peak at 1578 cm^{-1}, and the 2D peak at 2690 cm^{-1}, compared to the absence of these three peaks for the PI film (Fig. 2b). Besides the typical characteristic G and 2D peaks of graphene, the D peak represents the disordered vibration peak of graphene, which indicates the possible occurrence of partial oxidation and formation of defects during laser scribing in the ambient environment (Avinash and Patolsky, 2023; Ferrari and Robertson, 2000; Mahapatra et al., 2024). The *in situ* galvanic reduction process (Onisuru et al., 2020) was adopted to modify LIG electrodes with AuNC to enable the non-enzymatic sensing capability toward glucose. The successful deposition of AuNC on LIG is further confirmed by SEM combined with EDS (Fig. 2a), XRD (Fig. 2c), and XPS (Fig. 2d). With *in situ* galvanic reduction, the amount and morphology of AuNC can be well controlled by the concentration of $HAuCl_4{\cdot}3H_2O$ precursor solutions and the deposition time. For a fixed deposition time of 1 h, increasing the concentration *c* (in mg/mL) of $HAuCl_4{\cdot}3H_2O$ solutions transforms the AuNC morphology in the AuNC_*c*/LIG electrode from nanoparticles (with a diameter of ~60 nm) for AuNC_1/LIG to nanoflowers for AuNC_3/LIG. Further increasing the $HAuCl_4{\cdot}3H_2O$ solution concentration to 12 mg/mL leads to a dense nanoflake structure with reduced porosity, as shown in the SEM and EDS images. Without loss of generality, the AuNC_12/LIG electrode is adopted in the following investigation unless specified otherwise. Compared with the conventional electroplating and dip-coating method, galvanic reduction can provide much more uniform and stable metallic coatings on less-conductive porous substrates (Fig. S5) (Zahed et al., 2020; Tehrani and Bavarian, 2016; Zhu et al., 2021b). Meanwhile, the galvanic reduction-based modification is suitable for scalable production with high consistency and low sample-to-sample variations, as verified by the optical (Fig. S2) and SEM (Fig. S6) images of the AuNC/LIG electrode array fabricated in the same batch. The galvanic reduction-based modification technique doesn't introduce copper elements to the AuNC/LIG electrode, as revealed by the EDS mapping (Fig. S7).

The excellent electrochemical properties of AuNC/LIG electrodes

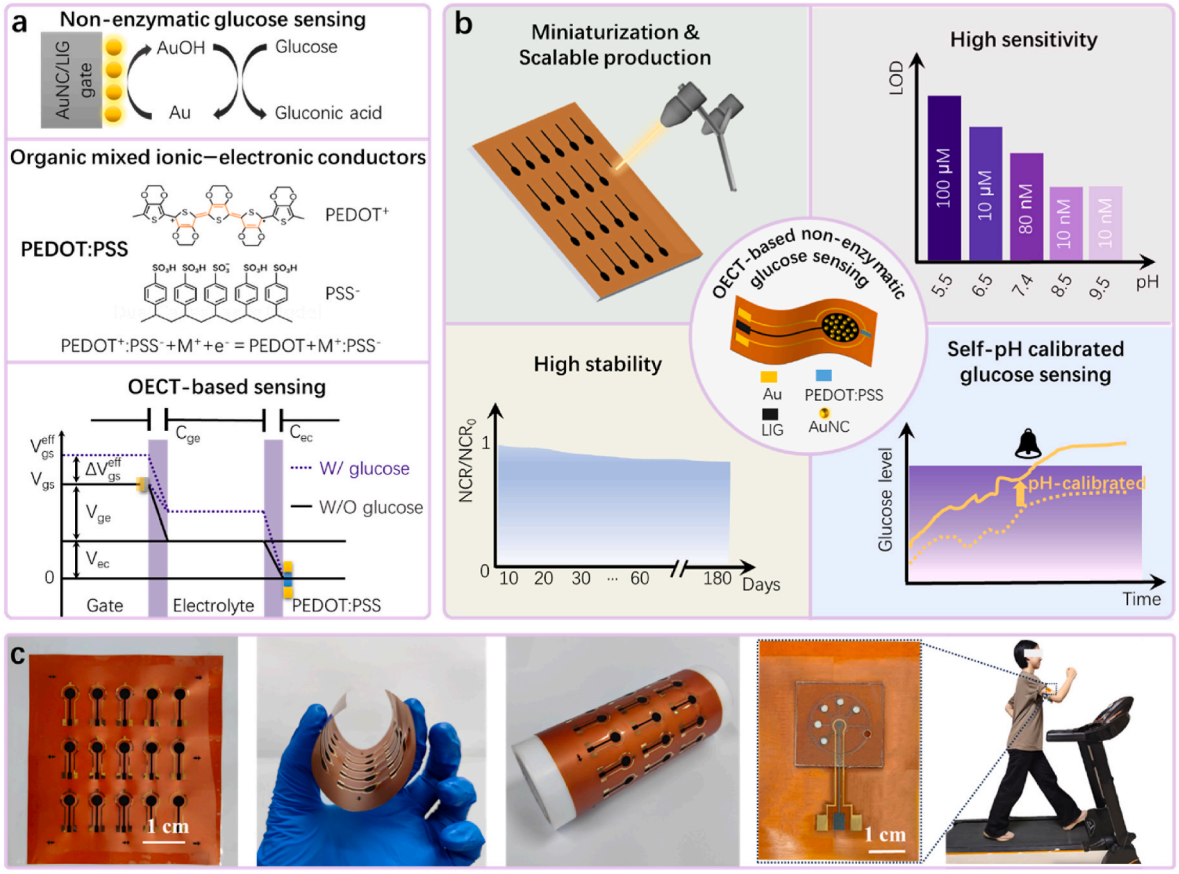

Fig. 1. Schematic illustrating the working principle and advantages of the non-enzymatic glucose sensor based on the OECT. (a) Schematics illustrating the glucose-sensing mechanism of the OECT-based non-enzymatic glucose, i.e., the carrier modulation of the PEDOT:PSS channel via the effective gate voltage, which is controlled by glucose oxidation at the AuNC/LIG electrode. **(b)** Schematic showing numerous advantages of the AuNC/LIG-gated OECT glucose sensor, including miniaturization and scalable production, high sensitivity, high stability over time, and self-pH calibration. **(c)** Optical images of the OECT-based non-enzymatic flexible glucose sensor array in the flat or bending state, as well as the integrated devices for non-invasive sweat glucose sensing.

were revealed from CV and EIS measurements in the three-electrode configuration. With the presence of the Fe^{2+}/Fe^{3+} redox couple in CV measurements, the corresponding oxidation and reduction peaks from the AuNC/LIG electrode are much higher than those from the planar Au (i.e., *p*_Au) and pristine LIG electrode (Fig. 2e), indicating much better electrochemical reactivity (Jeong et al., 2025). The charge-transfer resistance (R_{ct}) of the LIG electrode is larger than that of the *p*_Au electrode and it decreases from 310 Ω to 250 Ω after AuNC modifications (Fig. 2f). The LIG electrode shows a higher diffusion rate (as indicated by the slope of the linear curve at the lower frequency range) than the *p*_Au electrode due to its porous structure, and the AuNC modification on LIG further improves the diffusion rate. The high charge transfer rate from AuNC modifications and the large specific areas of porous LIG result in the extraordinary glucose sensing performance of the AuNC/LIG electrode. Moreover, the EIS of ten AuNC/LIG electrodes fabricated from the same batch shows a small sample-to-sample variation (~2.2 %) (Fig. S8). The sensing performance of samples from different batches also features a small variation of ~3.4 % (Fig. S9). These results confirm the highly controllable and consistent modification based on galvanic reduction. The AuNC/LIG electrode exhibits clear oxidation-reduction peaks to the added 5 mM glucose in CV measurements (Fig. 2g). With a pH value of 13, the adsorption of OH^- on the surface of AuNC leads to the formation of $AuOH_{ads}$ during the positive scan, which serves as the catalytic site for glucose oxidation. The relatively broad anodic peak at −0.1 V ("I") represents the oxidation of glucose into the intermediate product (i.e., gluconolactone). As the applied potential increases, gluconolactone is further oxidized into gluconate at 0.45 V ("II"). The formation of oxide on the AuNC surface above 0.45 V reduces $AuOH_{ads}$ active sites, leading to a decrease in the anodic peak current. During the negative scan, the reduction of Au oxides regenerates sufficient $AuOH_{ads}$ for glucose oxidation, manifesting by a significant anodic peak at 0.3 V (Chiu et al. 2020a, 2020b; Xu et al., 2017; Thanh et al., 2016b). A peak at about −0.2 V was observed in both cases (i.e., with or without glucose additions), which can be attributed to the reduction of the $AuOH_{ads}$ (Chiu et al., 2020a; Xu et al., 2017). The increased peak current with the increasing pH value confirms the improved electrochemical reactivity of the AuNC/LIG electrode toward glucose in alkaline environments. Notably, the glucose oxidation peaks almost vanish as pH decreases to 7.4 due to the low reaction kinetics (Fig. S10), which accounts for the degraded glucose sensing performance of non-enzymatic sensors with traditional three-electrode configurations in near-neutral biological fluids.

3.3. Characterization of the OECT-based non-enzymatic glucose sensor

The OECT-based non-enzymatic glucose sensor introduced in this work features an in-plane gating structure (Fig. 3a). As the channel material of the OECT, the p-type semiconducting PEDOT:PSS is in a highly conductive state under zero gate voltage due to the hopping of free electrons along the main chain of $PEDOT^+$. When a positive bias is applied, it changes to a low-conductivity state due to the injection of positive ions and the recombination of free electrons with $PEDOT^+$, leading to a de-doping effect that switches the OECT into depletion mode (Fan et al., 2019; Pappa et al.). Therefore, the input electrical signal on the gate electrode is amplified by the channel current (i.e., the drain-source current, I_{ds}) through the high transconductance of the

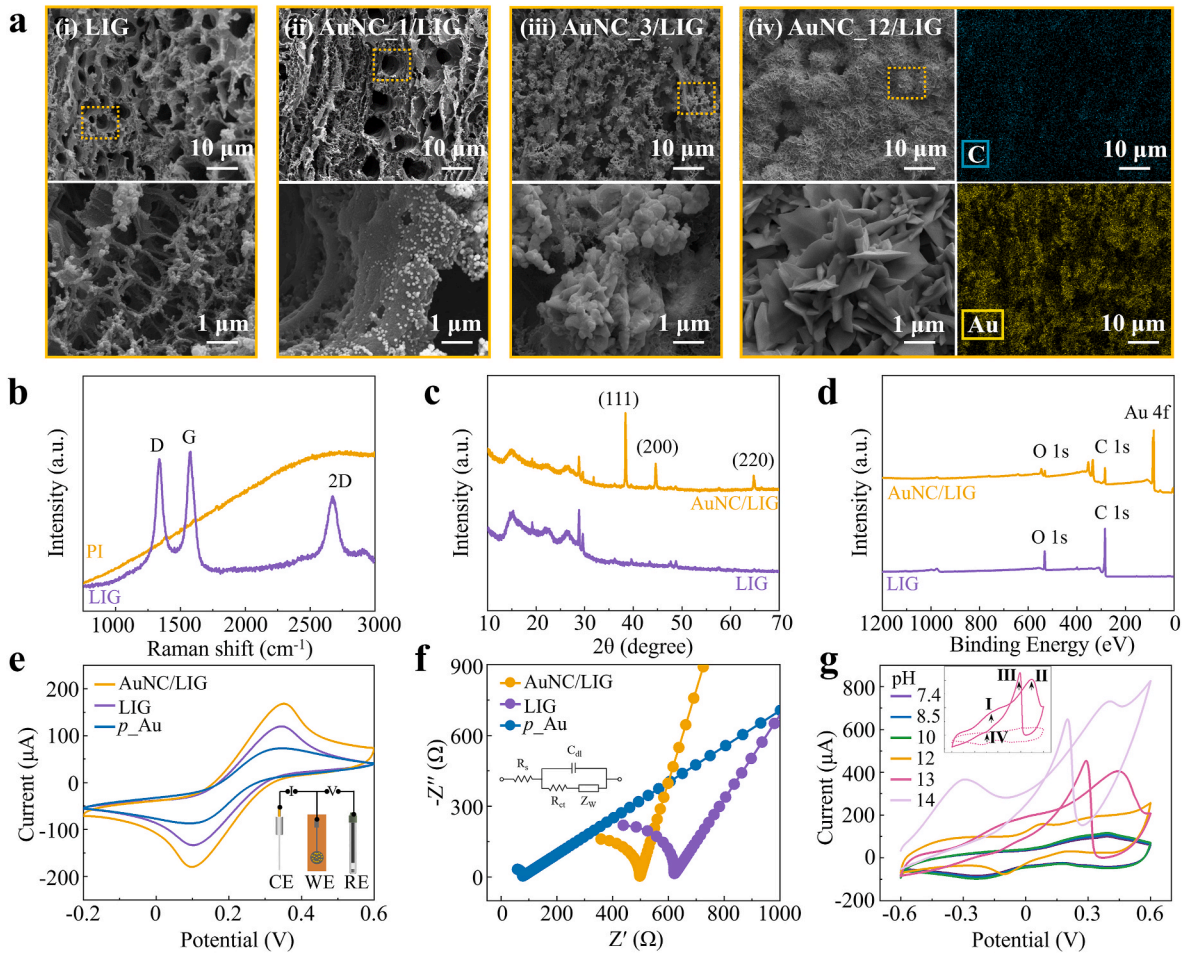

Fig. 2. Characterization of LIG and AuNC/LIG gate electrodes. (a) SEM images of the **(i)** LIG, **(ii)** AuNC_1/LIG, **(iii)** AuNC_3/LIG, **(iv)** AuNC_12/LIG electrode, along with the EDS mapping of AuNC_12/LIG electrode. **(b)** Raman spectrum of the polyimide (PI) film and the LIG electrode. **(c)** XRD and **(d)** XPS of the LIG and AuNC/LIG electrodes. **(e)** CV and **(f)** EIS curves of the LIG, AuNC/LIG, and planar Au (*p*_Au) electrode measured in 5 mM $[Fe(CN)_6]^{3-/4-}$ redox probe. EIS measurements were carried out at 0.35 V in the frequency range from 0.01 Hz to 1000 kHz. The inset shows the Randles circuit for fitting the Nyquist plots. **(g)** CV curves of the AuNC/LIG electrode after adding 5 mM glucose in different pH solutions. The inset shows the magnified CV curve with (solid) or without (dashed) 5 mM glucose (pH = 13).

OECT. As the glucose concentration alters the effective gate voltage due to the faradaic process, accurate glucose concentrations can be measured from the amplified I_{ds} change in the OECT with AuNC/LIG gate electrodes.

As the glucose sensing performance relies on the amplification effect of the OECT, the intrinsic transfer and transconductance characteristics of the PEDOT:PSS-based OECT with a channel length of 0.1 mm and width of 2 mm are first investigated for various gate electrodes: commercial Ag/AgCl, LIG, AuNC/LIG, and *p*_Au electrodes. Gated by an Ag/AgCl electrode, the PEDOT:PSS-based OECT maintains an on-off behavior and almost unchanged cut-off voltage in both acidic and basic solutions (Fig. 3b), indicating its robust performance in various pH environments. However, the on-state conductivity decreases with increasing pH, which can be attributed to the disruption of the π-π stacking structure of $PEDOT^+$ chains due to their neutralization with OH^- in the solution (Lee et al., 2023; Mochizuki et al., 2012; Garreau et al., 2001). The pH-dependent on-state conductivity can be leveraged to measure the pH value of biofluids and calibrate glucose sensing results for improved accuracy. The OECT gated by polarized electrodes (e.g., LIG, AuNC/LIG, and *p*_Au) exhibits similar on-off behaviors (Fig. 3c), but with a right-shifted threshold voltage (Fig. 3d). The effective voltage applied on the channel (V_{ec}) can be expressed by $V_{ec} = \frac{V_{gs}}{C_{ec}/C_{ge}+1}$, where V_{gs} is the gate voltage and C_{ec} (C_{ge}) is the capacitance at the electrolyte/channel (gate/electrolyte) interface. Non-polarized electrodes (i.e., Ag/AgCl) exhibit a larger C_{ge} due to fast charge transfer in Faradaic processes at the gate/electrolyte interface, and thus result in a higher V_{ec} for the same V_{gs}, compared to polarized electrodes (i.e., LIG, AuNC/LIG, and *p*_Au) (Fig. S11) (Gao et al., 2024).

Compared to the *p*_Au electrodes, the LIG and AuNC/LIG electrodes with 3D porous structures provide a higher C_{ge}, resulting in a smaller shift of the threshold voltage and a leftward shift in the transfer curve of OECT. Nevertheless, the maximal transconductance (g_m) of OECT with different gate electrodes is still higher than 4 mS (Fig. S12) due to the volumetric doping of PEDOT:PSS, as described by

$$g_m = \frac{Wd}{L}\,\mu\,C^*\,(V_{th} - V_{gs}) \tag{1}$$

where W, L, and d are the channel width, length, and thickness of OECT, μ is the carrier mobility of PEDOT:PSS, C^* is the specific volumetric capacitance, and V_{th} is the threshold gate voltage (Yao et al., 2023). The high transconductance of OECT ensures an excellent amplification effect for low-concentration biosensing.

Since FET or OECT-based biosensors do not exhibit a linear response like conventional electrochemical or optical sensors, the normalized current response (NCR) is defined as the ratio of the drain current before (I_{ds}^0) and after (I_{ds}^c), the addition of glucose with a given concentration of c as follows (Bernards et al., 2008):

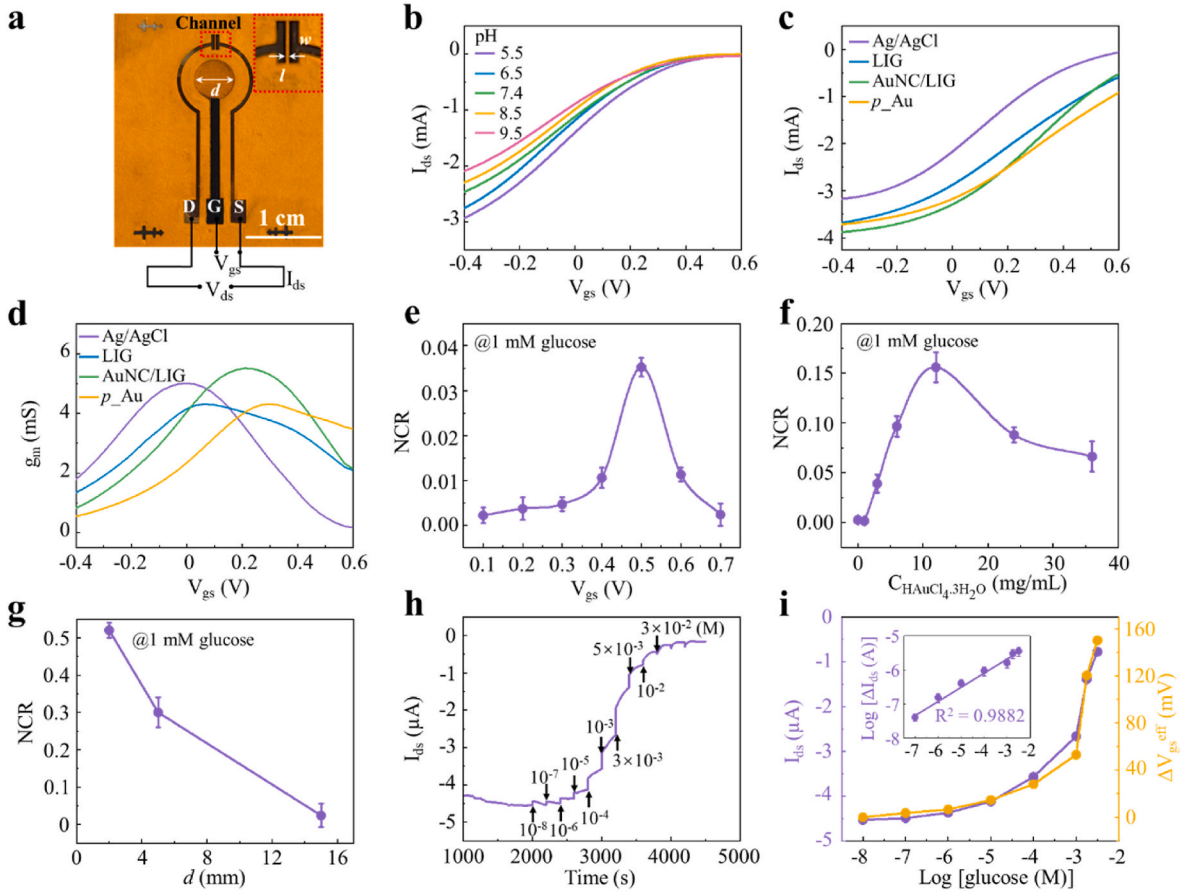

Fig. 3. Characterization and optimization of the OECT-based non-enzymatic glucose sensor. (a) Optical images of the OECT-based non-enzymatic glucose sensor. The channel dimensions are defined as L (length) × W (width). **(b)** Transfer curves of the OECT gated by an Ag/AgCl reference electrode in solutions with different pH values. **(c)** Transfer and **(d)** transconductance curves of the OECT in a PBS solution (pH = 7.4) with different gate electrodes: the Ag/AgCl, LIG, AuNC/LIG, and *p*_Au electrode. The influence of **(e)** the applied gate voltage, **(f)** AuNC loadings, and **(g)** gate electrode size on the normalized current response (NCR) of the OECT-based non-enzymatic glucose sensor to 1 mM glucose (pH = 7.4). **(h)** Typical amperometric response of the optimized OECT-based non-enzymatic glucose sensor to progressively added glucose from 10^{-8} M to 30 mM (pH = 7.4). **(i)** Current response and effective gate potential shift of the optimized OECT-based non-enzymatic glucose sensor as a function of the glucose concentration. Inset is the current response change plotted on a logarithmic scale. All data points are represented as means ± standard deviation (SD) from five samples.

$$NCR = \left| \frac{I_{ds}^{c} - I_{ds}^{0}}{I_{ds}^{0}} \right| \quad (2)$$

to provide a fair comparison of sensitivity for OECT-based biosensors.

The applied gate voltage, AuNC loadings on the LIG electrode, and gate electrode size of the OECT-based non-enzymatic glucose sensor can be optimized for enhanced sensitivity, LOD, and working range to match with various biofluids, such as sweat, saliva, and blood serum (Table S1). The applied voltage influences not only the electrochemical reactivity but also the transconductance, thereby affecting the amplification effect. A low gate voltage is insufficient to electrochemically oxidize glucose, whereas a high gate voltage is unfavorable for high amplification and also reduces selectivity due to the oxidation of interferents. Therefore, it is essential to optimize the applied gate voltage on AuNC/LIG in the OECT for highly sensitive glucose detection. With a progressive rise in glucose concentrations, increasing the gate voltage from 0.1 to 0.7 V decreases the initial current magnitude of the AuNC/LIG-gated OECT (Fig. S13), which is attributed to the intrinsic depletion mode of PEDOT:PSS-based OECT (Liang et al., 2021). The NCR of the AuNC/LIG-gated OECT initially increases and then decreases as the applied gate voltage increases from 0.1 to 0.7 V, with the highest NCR obtained at 0.5 V for 1 mM glucose (Fig. 3e). The optimal applied potential of 0.5 V for sensitivity is higher than 0.2 V for the maximal transconductance and 0.3 V for glucose oxidation by $AuOH_{ads}$, which can be attributed to the coexistence of the faradaic (i.e., the glucose oxidation) and non-faradaic (i.e., the formation of interfacial double layers) process at the gate/electrolyte interface.

As the concentration of $HAuCl_4{\cdot}3H_2O$ precursor solutions during the galvanic reduction process affects the amount and morphology of AuNC loadings on the LIG, it is also optimized to improve NCR of AuNC/LIG-gated OECT for glucose sensing (Fig. S14). The negligible response of the pristine LIG (without AuNC modification) to glucose confirms the key role of AuNC in non-enzymatic glucose sensing. The NCR of AuNC/LIG-gated OECT to 1 mM glucose initially increases and then decreases with the $HAuCl_4{\cdot}3H_2O$ concentration, with the highest NCR achieved at 12 mg/mL (i.e., AuNC_12/LIG) (Fig. 3f). For a fixed size of channels, increasing the size of the AuNC/LIG gate electrode reduces the NCR but extends the working range. The increase in gate electrode size, accompanied by an increase in C_{ge}, results in a leftward shift in the transfer and transconductance curves of the OECT (Fig. S15). It is found that the NCR of AuNC/LIG-gated OECT for 1 mM glucose decreases with increasing gate electrode size (Fig. 3g). Considering the wide range of glucose concentrations in biofluids (from 28 μM to 8 mM) (Boselli et al., 2021; Niu et al., 2013), the AuNC/LIG gate electrode in the OECT is designed with a diameter (i.e., d) of 5 mm to cover this range while maintaining an optimized NCR.

With the aforementioned optimized parameters, the sensing perfor-

mance of the AuNC/LIG-gated OECT glucose sensor is characterized by dropwise addition of glucose solutions (10^{-8} M to 3×10^{-2} M), with a significant response observed until saturation at ~30 mM (Fig. 3h). The gate current (i.e., I_{gs}) of the OECT remains consistently low at 10^{-8} A and shows almost no change with glucose addition, confirming that the high sensitivity originated from the transconductance of the OECT (Fig. S16). The glucose sensor shows an exponential relationship between I_{ds} and glucose concentration on a logarithmic scale (Fig. 3i), which is an intrinsic property of FET-based sensors (Tang et al., 2011; Wang et al.; Nakatsuka et al., 2018). However, changing the y-axis (i.e., ΔI_{ds}) into the logarithmic scale (i.e., Log [ΔI_{ds}(A)]) yields a linear calibration curve to facilitate practical applications (see the inset of Fig. 3i). The increased glucose oxidation at high concentrations results in more charge transfer in the faradaic process, leading to a reduction in V_{ge} and a consequent leftward shift in the output curve (Fig. S17). The effective gate voltage V_{gs}^{eff} that will lead to the same V_{ec} without glucose additions can be given by the following equation (Tang et al., 2011):

$$V_{gs}^{eff} = V_{GS} + (C_{ec} / C_{ge} + 1)\frac{kT}{2q} \ln[glucose] + constant \quad (3)$$

where k is the Boltzmann constant, T is the temperature, q is the electron charge, and C is a constant. The shift in the effective gate voltage (ΔV_{gs}^{eff}) as a function of glucose concentration, derived from the channel current using the normalized transfer curve, follows the same trend as I_{ds} but deviates from the analytical equation (Fig. 3i). This finding is consistent with previous results in the OECT-based nitric oxide sensor (Deng et al., 2022) and the FET-based dopamine sensors (Zhang et al., 2014a), which can be attributed to the weak reaction of glucose in near-neutral conditions. Consistent with these works, a linear correlation (R^2 of 0.9984) between glucose concentration and ΔV_{gs}^{eff} can be established by changing to logarithmic scale (Fig. S18).

3.4. Comparison of sensing performance

The combination of non-enzymatic and OECT-based sensing mechanisms offers the advantages such as superior LOD and long-term and temperature stability, which was highlighted by comparison with the three-electrode-based non-enzymatic and OECT-based enzymatic sensors (Fig. 4a). The NCR of OECT-based glucose sensors increases before reaching saturation with glucose concentrations in alkaline solutions (e.g., pH = 8.5 and 9.5) (Fig. 4b), which is consistent with previous work (Cicoira et al., 2010). Impressively, the NCR of AuNC/LIG-gated OECT at low glucose concentrations (e.g., 10^{-8} - 10^{-6} M) increases significantly with pH (Fig. S19), which can be attributed to the enhanced

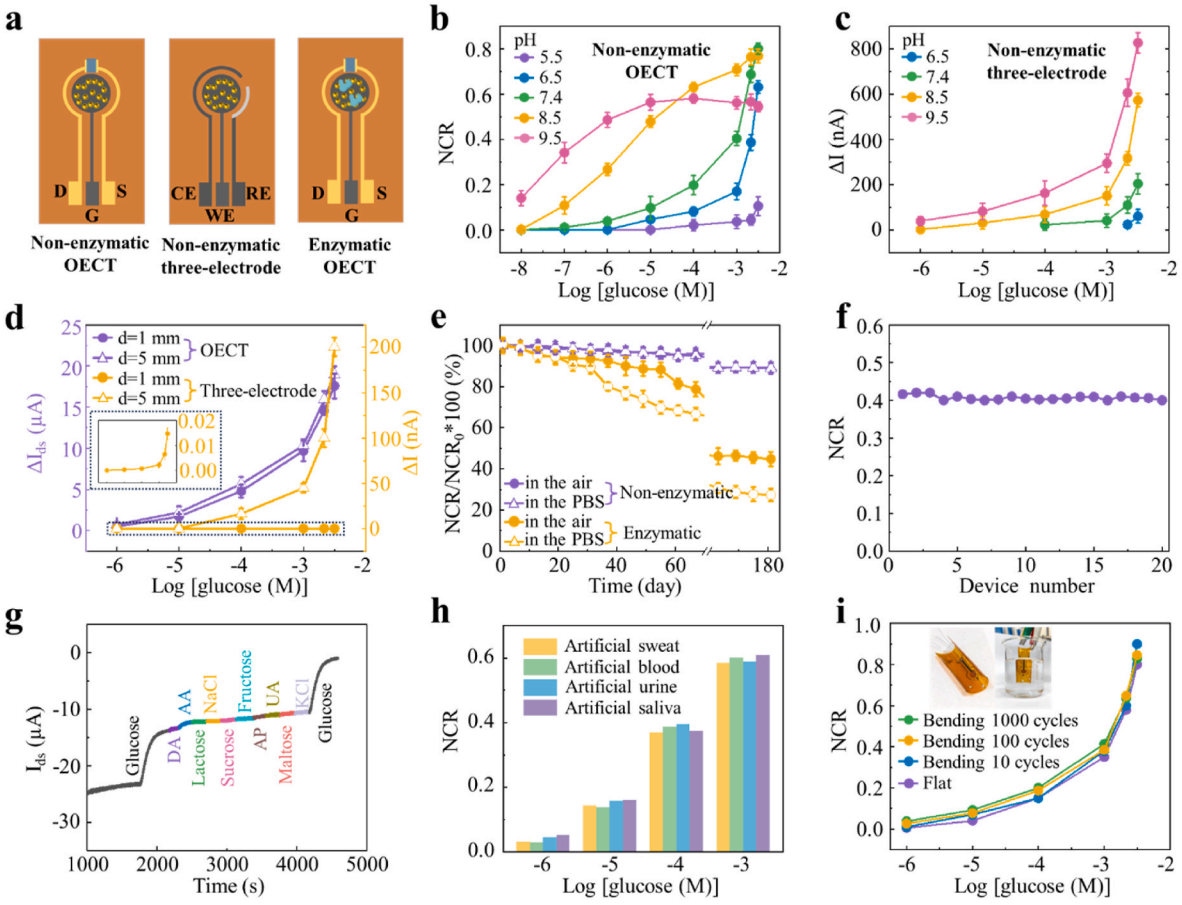

Fig. 4. Sensing performance of the OECT-based non-enzymatic glucose sensor. (a) Schematic diagram of the OECT-based non-enzymatic, three-electrode-based non-enzymatic, and OECT-based enzymatic glucose sensor. **(b)** NCR of the AuNC/LIG-gated OECT and **(c)** amperometric response of the bare AuNC/LIG electrode in the three-electrode configuration at different pH levels. **(d)** Current response of the OECT or three-electrode-based non-enzymatic glucose sensor with reduced AuNC/LIG electrode sizes. **(e)** Comparison of the long-term stability of the OECT-based enzymatic and non-enzymatic glucose sensor over 180 days in air and PBS solution. **(f)** NCR of twenty AuNC/LIG-gated OECT glucose sensors fabricated in the same batch to additions of 1 mM glucose. **(g)** Selectivity test of the OECT-based non-enzymatic glucose sensor with various interferents, including DA, AA, lactose, NaCl, KCl, sucrose, fructose, maltose, AP, and UA. **(h)** NCR of the OECT-based non-enzymatic glucose sensor tested in different artificial biofluids (i.e., artificial sweat, blood, urine, saliva, and sweat) with increasing glucose concentrations from 10^{-6} M to 10^{-3} M **(i)** NCR of OECT-based non-enzymatic glucose sensor to glucose additions before and after repeated bending of 10, 100, and 1000 cycles. The inset shows the optical image of the flexible glucose sensor in the bending state with a radius of 10 mm. All data points are represented as means ± standard deviation (SD) from five measurements.

electrochemical activity of non-enzymatic AuNC/LIG electrodes in alkaline environments. Besides high sensitivity, the LOD and working range of the optimized OECT-based glucose sensor are also important for glucose detection from various biofluids. Similar to the NCR, the LOD of OECT-based glucose sensors is lower in alkaline environments. In contrast, the maximal measurable glucose concentration (i.e., the saturation point of the NCR curve) decreases with increasing pH. For example, the LOD and maximal measurable glucose concentration of AuNC/LIG-gated OECT at pH = 9.5 (6.5) are 0.01 (10) μM and 0.1 (>5) mM, respectively. As expected, the AuNC/LIG electrode in the three-electrode configuration also favors basic environments for glucose sensing, as revealed by the lower LOD at higher pH values (Fig. 4c, Fig. S20). The experimentally measured LOD of the OECT-based sensor is more than two orders of magnitude lower than that of the non-enzymatic sensor with a three-electrode configuration, while maintaining the same AuNC/LIG electrode dimensions (Table S2), confirming the key role of the amplification effect from the transconductance of OECT. The theoretical LOD of the OECT-based glucose sensor reaches as low as ~0.08 μM in near-neutral solutions (i.e., PBS with pH = 7.4), which enables direct and continuous glucose sensing in biofluids. This value is also much lower than the other metal nanoparticle-based non-enzymatic glucose sensors reported by previous studies (Table S3). Notably, the OECT with the non-enzymatic electrode (i.e., AuNC/LIG) exhibits higher NCR values than that with the enzymatic electrode (GOx/AuNC/LIG) for the same OECT configuration (Fig. S21).

Another salient advantage of OECT-based glucose sensors is facile miniaturization (with reduced overall sensor dimensions) without compromising sensing performance, while also minimizing the volume of biofluids required for rapid sampling and sensing. As the working electrode size decreases from 5 mm to 1 mm, the conventional electrochemical sensor with the three-electrode configuration shows a significantly reduced current response by more than four orders of magnitude (Fig. 4d). In contrast, the OECT-based glucose sensor with a reduced channel length, width, and gate electrode by 1/5 (while fixing the gate/channel ratio, Fig. S22) maintains an almost unchanged sensing curve. The uncompromised sensing performance with a dramatic size reduction facilitates the miniaturization of wearable devices for multimodal, high-density integration.

The long-term stability of the flexible AuNC/LIG-gated OECT glucose sensor is significantly higher than that of the OECT-based enzymatic sensor in both air and liquid environments (Fig. 4e). The degradation of the OECT-based enzymatic sensor is 30 % in air and 40 % in the PBS solution over the measurements of 20 days, whereas the NCR variation of the AuNC/LIG-gated OECT glucose sensor is less than 5 % in both air and PBS solution. The non-enzymatic OECT-based sensor also exhibits extremely high stability, with degradation of only ~10 % even over an extended period of up to 180 days (Table S4), benefiting from its reference electrode-free and enzyme-free design. Additionally, negligible variations in the sensing performance of the OECT-based glucose sensor under temperature fluctuations were observed (Fig. S23). Without the involvement of enzymes, the low-cost AuNC/LIG-gated OECTs, with their superior long-term stability, eliminate the need for frequent calibration or sensor replacement, thereby reducing overall costs. The flexible OECT-based glucose sensor, fabricated using laser scribing and galvanic reduction-based modification, demonstrates very low sample-to-sample variation, as evidenced by a relative standard deviation (RSD) of 2.07 % in the NCR among twenty glucose sensing units from the same batch (Fig. 4f). This confirms the high consistency, uniformity, and controllability of the fabrication process.

Considering the complex chemical compositions in biofluids, it is necessary to evaluate the specificity of the AuNC/LIG-gated OECT glucose sensor against common inorganic and organic interfering agents, including NaCl, KCl, various monosaccharides (e.g., sucrose, maltose, and fructose), dopamine (DA), ascorbic acid (AA), 4-acetamidophenol (AP), uric acid (UA), and lactose (Fig. 4g, Fig. S24). Monosaccharides were selected to test the specific sensing mechanism of AuNC/LIG electrodes, while the choice of other interfering agents and their concentrations was based on the composition and typical concentration ranges in the biofluid being tested, such as sweat in this work. The negligible response of the OECT-based biosensor to other monosaccharides confirms its specificity for glucose. Compared to glucose, DA, AP, and UA, which have similar oxidation potentials, result in a much smaller current response (NCR ~ 0.02). Although AA is a well-known interferent due to its high reductivity, the use of a Nafion layer on the AuNC/LIG electrode significantly reduces AA interference by leveraging electrostatic repulsion (Zhu et al., 2021a; Zhang et al., 2014b). Lactose, even at high concentrations, produces almost no current response. Additionally, the OECT-based non-enzymatic glucose sensor recovers to its initial state within 5 min after glucose removal (Fig. S25), indicating excellent reversibility. Its high selectivity and specificity were further verified in different artificial biofluids such as artificial sweat, blood, urine, and saliva (pH = 7.4). Despite the complex composition of these artificial fluids (Table S5), the OECT-based non-enzymatic biosensor shows a consistent response with negligible variations (Fig. 4h, Fig. S26). Furthermore, the OECT-based non-enzymatic glucose sensor demonstrates excellent mechanical robustness, as evidenced by minimal NCR changes (<4.6 %) under bending deformations with a radius of 10 mm (Fig. 4i, Fig. S27).

It is important to note that the pH level of biofluids may vary significantly with the physiological conditions of different individuals. For example, human sweat, which is weakly acidic or neutral under normal conditions, becomes weakly alkaline as the heart rate increases during exercise (Granger et al., 2003). Due to these pH fluctuations, the sensing performance of the AuNC/LIG-gated OECT glucose sensor is significantly affected, as confirmed by the characterization in artificial sweat (Fig. S28). To enable accurate glucose sensing in biofluids with dynamically changing pH values, and to provide a comprehensive evaluation of physiological conditions, a simple yet effective self-pH calibration method can be implemented within the OECT-based glucose sensor without the need for additional pH sensing units. The working principle relies on the pH-dependent conductivity of PEDOT:PSS. The pH calibration based on PEDOT:PSS exhibits high stability under varying environmental conditions and during extended use for one month (Fig. S29). In particular, the conductance of the PEDOT:PSS-based channel at zero gate voltage (i.e., I_{ds} at V_{gs} = 0 V) can be used to determine the pH value (Fig. S30). Next, by measuring the drain current at an applied gate voltage of 0.5 V (i.e., I_{ds} at V_{gs} = 0.5 V) and referencing the calibration curve at the determined pH value, the glucose concentration can be obtained with significantly improved accuracy. The two-step measurement with self-pH calibration can be iterated during continuous glucose monitoring in case of frequent and dramatic pH fluctuations.

3.5. Integrated OECT-based devices for real-time sweat glucose sensing and correlation studies

Integrating the AuNC/LIG-gated OECT with a microfluidic module enables the development of a wearable glucose sensor for real-time sampling and monitoring of sweat on human skin (Fig. 5a). The correlation between sweat and blood glucose concentrations can be established by measuring blood glucose levels at specific time points using a commercial finger-prick-based sensor. The AuNC/LIG-gated OECT-based glucose sensing layer is sandwiched between a bottom sweat inlet layer and a top microfluidic layer below an outlet layer. The microfluidic channel and detection chamber are fabricated by highly efficient laser patterning of hydrophilic polyethylene glycol terephthalate (PET) films. Capillary forces drive sweat flow along the microfluidic channel into an ultra-small chamber with an area of 8.9 mm^2. With red-dyed ink for easy visualization, the fluid flow at a rate of 637 μL min^{-1} cm^{-2} (higher than the typical sweat rate of 61.9 μL min^{-1} cm^{-2}) takes 100 s to fill on inlet microfluidic channel and chamber with a volume of 8.4 μL (Fig. 5b), due

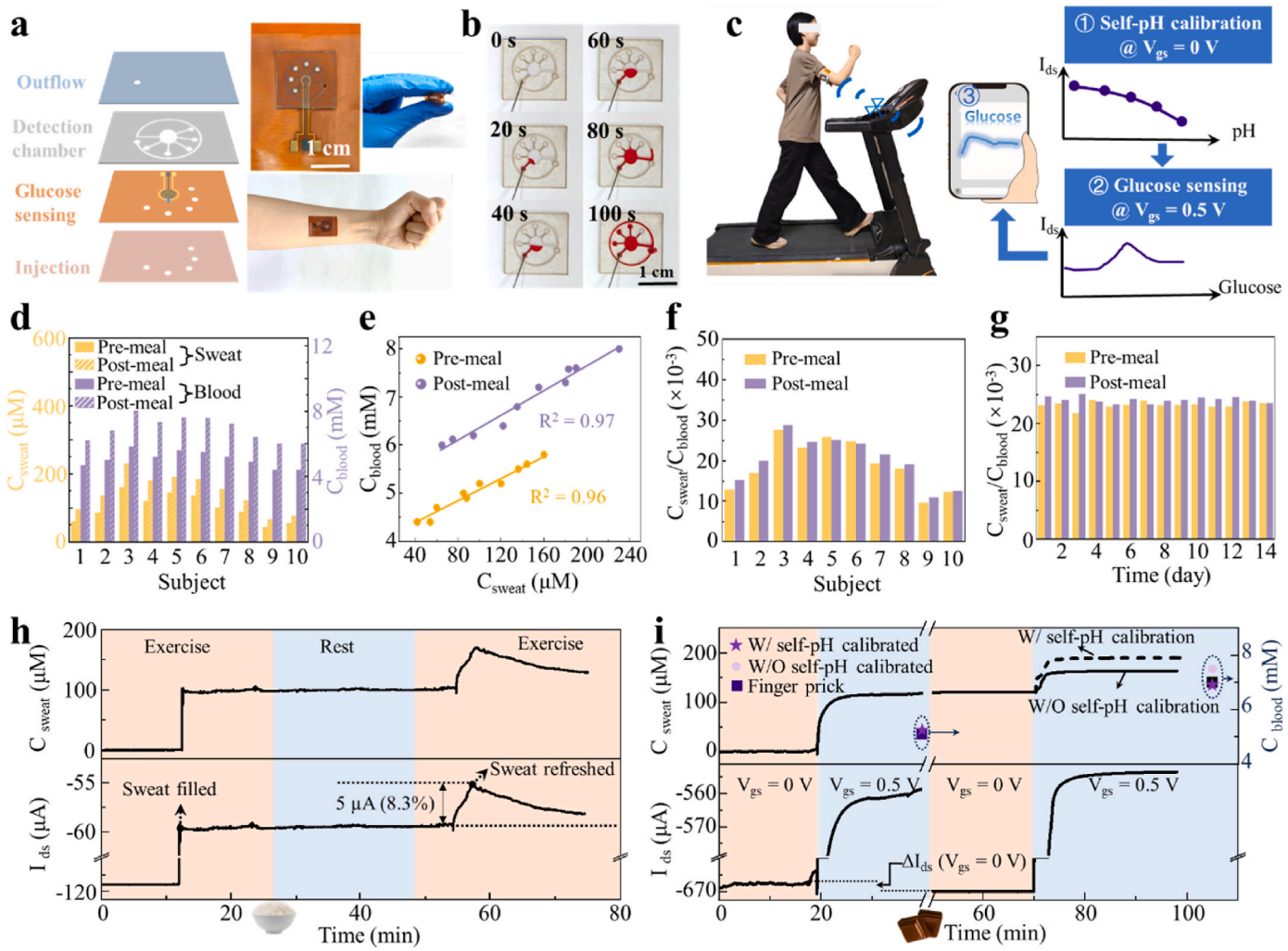

Fig. 5. Fully integrated, wearable, OECT-based sweat sensors for real-time glucose monitoring. (a) Exploded view (left) and optical images (right) of the fully integrated, wearable, OECT-based sweat glucose sensor. **(b)** Optical images of the microfluidic module at different time points show the fluid sampling process. **(c)** Schematic of the two-step measurement with pH calibration for real-time, continuous glucose monitoring using the fully integrated sweat glucose sensor, which includes a built-in Bluetooth module for wireless data transmission. **(d)** Comparison of glucose levels in sweat (measured by the OECT-based glucose sensor) and blood (measured by a commercial finger-prick glucose meter) from ten subjects before and after meals. **(e)** Correlations between glucose levels in blood and sweat before and after meals. **(f)** Correlations between glucose levels in blood and sweat for each subject before and after meals. **(g)** Correlations between glucose levels in the blood and sweat of human subject #4 over a 14-day measurement period. Real-time, continuous measurements of sweat glucose levels from human subject #4 before and after the intake of **(h)** rice and **(i)** chocolate, along with the measured glucose level in the blood. The intake of chocolate causes a pH change, which can be self-calibrated by the same sensing unit for improved accuracy of sweat/blood glucose concentrations.

to the good hydrophilicity properties of the PET film. The small size of the OECT, combined with their uncompromised sensing performance, reduces the required volume of biofluid and enables the use of miniaturized microfluidic units. Moreover, iontophoresis-based transdermal delivery of sweat stimulants (e.g., acetylcholine, pilocarpine, bethanechol, methacholine, and carbachol) can induce continuous sweat production on various parts of the human body without the need for exercise (Sempionatto et al., 2021; Xu et al., 2024), which can greatly extend the application scenario of the OECT-based glucose sensors. The flexible PET and PI materials provide the integrated sweat sensor with robust performance against bending, allowing it to conformally attach to human skin with an adhesive layer for reliable glucose measurements even during motion. By combining the integrated sensor with a miniaturized 2-channel electrochemical station equipped with a built-in Bluetooth module, the measured data can be wirelessly transmitted to portable devices, such as smartphones and tablets (Fig. 5c). Additionally, the aforementioned self-pH calibration is implemented to enhance the accuracy of glucose measurements in dynamic environments.

Evaluation of the fully integrated sweat glucose sensor in vivo on ten healthy human subjects demonstrates its feasibility for practical applications. Each subject engaged in a light workout session (e.g., indoor running) for 30 min before and after meals, to generate sweat for glucose measurements, while blood glucose levels were also simultaneously measured using a commercial finger-prick glucose meter (Fig. 5d), a strong linear correlation between sweat and blood glucose levels was observed for all ten human subjects ($R^2 = 0.97$ or 0.96) before and after the meal (Fig. 5e). Despite individual variations, the correlation between the sweat and blood glucose levels (i.e., C_{sweat}/C_{blood}) for each human subject remained nearly constant before and after the meal, with a negligible difference (<5 %) (Fig. 5f). For a specific subject (subject #4), C_{sweat}/C_{blood} remained consistent at $(23.6164 \pm 0.6620) \times 10^{-3}$ over a week of measurements (Fig. 5g), confirming the feasibility of long-term longitudinal studies. After individual calibration or setting up a calibrated database from a large population, it is possible to continuously and longitudinally monitor blood/sweat glucose levels for individualized evaluations.

Evaluation of the integrated sweat patch during food intake and exercise demonstrates the effectiveness of self-pH calibration for real-

time, continuous glucose sensing. In Fig. 5h, the microfluidic chamber was initially empty and then filled with sweat in approximately 12 min, the ionic pathways enabled by the electrolyte allow the gate voltage (V_{gs} = 0.5 V) to be applied to the channel, resulting in a sharp change in I_{ds}. As a result, the sweat rate of the human subject during exercise is calculated to be approximately 0.47 μL min^{-1} per sweat gland, which is consistent with previous reports (Zhang et al., 2020). After rice intake and resting for 30 min, the current (I_{ds}) remains constant in this period due to sweat retained in the microfluidic chamber without refreshing. Re-engaging in workouts after rest continues to stimulate sweat. As the channel is completely refreshed with new sweat, I_{ds} gradually decreases by 8.3 %, followed by a slow increase to a plateau higher than the pre-meal level. As a result, the sweat glucose concentration derived from the calibration curve increases from 100 to 170 μM after rice intake and then slowly decreases to 140 μM due to metabolic processes during exercise. Since there are negligible pH fluctuations and sweat rate changes during the entire measurement process after rice intake, a one-time pH determination at the beginning is sufficient for accurate glucose measurements. To highlight the self-pH calibration capability, the measurement started when the microfluidic chamber was filled with sweat or refreshed with new sweat after the intake of chocolate (Fig. 5i). A change in sweat pH from 6.5 to 6 after chocolate intake is detected by the PEDOT:PSS-based OECT at zero gate voltage, as revealed by a jump of the baseline current (ΔI_{ds}) (Fig. 5i). The measured pH change is consistent with that from the commercial pH meter, indicating the high accuracy of the PEDOT:PSS-based OECT for pH sensing. Due to the significant pH fluctuation, real-time pH calibration during continuous glucose monitoring becomes necessary. By using the *in situ* measured pH of 6 instead of the previously measured pH of 6.5, the glucose concentration in sweat is determined to decrease from 190 to 160 μM (using the calibration curve at pH = 6.0) (Fig. S31), corresponding to a decreased blood glucose concentration from 7.45 to 6.95 mM from the linear correlation. Compared to the blood glucose concentration of 7.0 mM measured by the commercial glucose meter, the self-pH calibration helps reduce the measurement error from 6.4 % down to 0.71 % by almost ten times. Considering that more dramatic pH changes are associated with larger measurement errors, it is crucial to utilize self-pH calibration for highly accurate glucose measurements in complex real-world scenarios over time, enabling informed clinical decisions. The OECT-based non-enzymatic glucose sensor for non-invasive continuous glucose sensing can be further integrated with insulin-loaded drug delivery systems, such as pumps or microneedles, to create a closed-loop system for managing diabetes in patients.

4. Conclusion

In summary, this work reports a wearable non-enzymatic OECT-based sweat glucose sensor gated by a porous, chemical-modified AuNC/LIG electrode with high sensitivity, specificity, and stability over time and fluctuations of pH/temperature. The highly controllable and consistent laser fabrication and *in situ* galvanic reduction process for chemical modifications hold great potential in scalable production and device miniaturization. The LOD of the non-enzymatic OECT-based glucose sensor can be as low as 0.08 μM at pH 7.4, surpassing all previously reported non-enzymatic glucose sensors and demonstrating its excellent applicability in near-neutral biological fluids. Across a wide pH range from 5.5 to 9.5, the LOD remains consistently two orders of magnitude lower than that of conventional electrochemical sensors with the three-electrode configuration. Besides the long-term stability, the OECT-based biosensor can perform self-pH calibration at zero gate voltage, first determining the pH value of biofluids and then accurately deriving glucose concentrations at the calibrated pH. Impressively, different from conventional electrochemical sensors with the "three-electrode" configuration, the OECT-based biosensor maintains uncompromised sensing performance even as its size is reduced, enabling the miniaturization of wearable devices. By combining the OECT-based non-enzymatic glucose sensor with the microfluidic module and miniaturized electrochemical workstation, the fully integrated glucose sensor can non-invasively and wirelessly detect sweat glucose levels that strongly correlate with blood glucose levels. The accurate measurement of sweat glucose by the non-enzymatic OECT-based biosensor, combined with self-pH calibration and its strong correlation to blood glucose levels, demonstrates the feasibility of this versatile platform for practical clinical applications across various food intake and physiological conditions.

CRediT authorship contribution statement

Ke Meng: Writing – review & editing, Writing – original draft, Visualization, Validation, Methodology, Investigation, Formal analysis, Data curation, Conceptualization. **Jia Zhu:** Writing – review & editing, Writing – original draft, Visualization, Validation, Supervision, Resources, Project administration, Methodology, Investigation, Funding acquisition, Formal analysis, Data curation, Conceptualization. **Tianyao Zhang:** Methodology, Investigation, Formal analysis, Data curation. **Xianzhe Zhang:** Writing – review & editing, Writing – original draft, Validation, Methodology, Investigation, Formal analysis, Data curation, Conceptualization. **Yingying Zhang:** Methodology, Investigation, Formal analysis, Data curation. **Xiangjie Chen:** Methodology, Investigation, Formal analysis, Data curation. **Fan Li:** Methodology, Investigation, Formal analysis, Data curation. **Yao Tong:** Methodology, Investigation, Formal analysis, Data curation. **Senhao Zhang:** Project administration, Methodology, Investigation, Formal analysis, Data curation. **Donghai Qiu:** Project administration, Methodology, Formal analysis, Data curation, Conceptualization. **Hongbo Yang:** Project administration, Methodology, Formal analysis, Conceptualization. **Shangbin Liu:** Methodology, Investigation, Formal analysis, Data curation. **Lan Yin:** Validation, Supervision, Conceptualization. **Rui Zhao:** Supervision, Investigation, Data curation, Conceptualization. **Libin Huang:** Supervision, Investigation, Data curation, Conceptualization. **Tao Li:** Supervision, Investigation, Data curation, Conceptualization. **Min Gao:** Supervision, Investigation, Formal analysis, Conceptualization. **Taisong Pan:** Supervision, Investigation, Formal analysis, Conceptualization. **Jian Yang:** Supervision, Project administration, Investigation, Formal analysis, Conceptualization. **Huanyu Cheng:** Writing – review & editing, Writing – original draft, Validation, Supervision, Resources, Project administration, Methodology, Investigation, Funding acquisition, Formal analysis, Data curation, Conceptualization. **Yuan Lin:** Writing – review & editing, Writing – original draft, Validation, Supervision, Resources, Project administration, Methodology, Investigation, Funding acquisition, Formal analysis, Data curation, Conceptualization.

Declaration of competing interest

The authors declare that they have no known competing financial interests or personal relationships that could have appeared to influence the work reported in this paper.

Acknowledgments

This work is supported by the Natural Science Foundation of China under grant Nos. 62301116, 62427806, U21A20460, and the Medico-Engineering Cooperation Funds, Fundamental Research Funds for the Central Universities, UESTC under grant No. ZYGX2021YGLH002. H.C. acknowledges the support provided by NIH (Award No. R21EB030140), NSF (Grant Nos. 2309323, 2243979, and 2319139), and Penn State University.

Appendix A. Supplementary data

Supplementary data to this article can be found online at https://doi.

org/10.1016/j.bios.2025.117677.

Data availability

Data will be made available on request.

References

Ahmed, I., Jiang, N., Shao, X., Elsherif, M., Alam, F., Salih, A., Butt, H., Yetisen, A.K., 2022. Recent advances in optical sensors for continuous glucose monitoring. Sens. Diagn. 1 (6), 1098–1125.

Avinash, K., Patolsky, F., 2023. Laser-induced graphene structures: from synthesis and applications to future prospects. Mater. Today 70, 104–136.

Baghayeri, M., Veisi, H., Ghanei-Motlagh, M., 2017. Amperometric glucose biosensor based on immobilization of glucose oxidase on a magnetic glassy carbon electrode modified with a novel magnetic nanocomposite. Sensor. Actuator. B Chem. 249, 321–330.

Bai, X., Chen, W., Song, Y., Zhang, J., Ge, R., Wei, W., Jiao, Z., Sun, Y., 2017. Nickel-copper oxide nanowires for highly sensitive sensing of glucose. Appl. Surf. Sci. 420, 927–934.

Bakhshandeh, F., Zheng, H., Barra, N.G., Sadeghzadeh, S., Ausri, I., Sen, P., Keyvani, F., Rahman, F., Quadrilatero, J., Liu, J., Schertzer, J.D., Soleymani, L., Poudineh, M., 2024. Wearable aptalyzer integrates microneedle and electrochemical sensing for in vivo monitoring of glucose and lactate in live animals. Adv. Mater. 36 (35), 2313743.

Benedetti, T.M., Somerville, S.V., Wordsworth, J., Yamamoto, Y., Schuhmann, W., Tilley, R.D., Gooding, J.J., 2024. An artificial enzyme: how nanoconfinement allows the selective electrochemical detection of glucose directly in whole blood. Adv. Funct. Mater. 34 (30), 2400322.

Bernards, D.A., Macaya, D.J., Nikolou, M., DeFranco, J.A., Takamatsu, S., Malliaras, G. G., 2008. Enzymatic sensing with organic electrochemical transistors. J. Mater. Chem. 18 (1), 116–120.

Boselli, L., Pomili, T., Donati, P., Pompa, P.P., 2021. Nanosensors for visual detection of glucose in biofluids: are we ready for instrument-free home-testing? Materials (Basel) 14 (8).

Chen, Y., Lu, S., Zhang, S., Li, Y., Qu, Z., Chen, Y., Lu, B., Wang, X., Feng, X., Skin-like biosensor system via electrochemical channels for noninvasive blood glucose monitoring. Sci. Adv. 3(12), e1701629.

Chen, Y., Sun, Y., Li, Y., Wen, Z., Peng, X., He, Y., Hou, Y., Fan, J., Zang, G., Zhang, Y., 2024. A wearable non-enzymatic sensor for continuous monitoring of glucose in human sweat. Talanta 278, 126499.

Chiu, W.-T., Chang, T.-F.M., Sone, M., Tixier-Mita, A., Toshiyoshi, H., 2020a. Roles of TiO2 in the highly robust Au nanoparticles-TiO2 modified polyaniline electrode towards non-enzymatic sensing of glucose. Talanta 212, 120780.

Chiu, W.-T., Chang, T.-F.M., Sone, M., Tixier-Mita, A., Toshiyoshi, H., 2020b. Electrocatalytic activity enhancement of Au NPs-TiO2 electrode via a facile redistribution process towards the non-enzymatic glucose sensors. Sensor. Actuator. B Chem. 319, 128279.

Cicoira, F., Sessolo, M., Yaghmazadeh, O., DeFranco, J.A., Yang, S.Y., Malliaras, G.G., 2010. Influence of device geometry on sensor characteristics of planar organic electrochemical transistors. Adv. Mater. 22 (9), 1012–1016.

Deng, Y., Qi, H., Ma, Y., Liu, S., Zhao, M., Guo, Z., Jie, Y., Zheng, R., Jing, J., Chen, K., Ding, H., Lv, G., Zhang, K., Li, R., Cheng, H., Zhao, L., Sheng, X., Zhang, M., Yin, L., 2022. A flexible and highly sensitive organic electrochemical transistor-based biosensor for continuous and wireless nitric oxide detection. Proc. Natl. Acad. Sci. 119 (34), e2208060119.

Fan, J., Rezaie, S.S., Facchini-Rakovich, M., Gudi, D., Montemagno, C., Gupta, M., 2019. Tuning PEDOT:PSS conductivity to obtain complementary organic electrochemical transistor. Org. Electron. 66, 148–155.

Farahmandpour, M., Haghshenas, H., Kordrostami, Z., 2022. Blood glucose sensing by back gated transistor strips sensitized by CuO hollow spheres and rGO. Sci. Rep. 12 (1), 21872.

Ferrari, A.C., Robertson, J., 2000. Interpretation of raman spectra of disordered and amorphous carbon. Phys. Rev. B 61 (20), 14095–14107.

Ferri, S., Kojima, K., Sode, K., 2011. Review of glucose oxidases and glucose dehydrogenases: a bird's eye view of glucose sensing enzymes. J. Diabetes Sci. Technol. 5 (5), 1068–1076.

Gao, L., Wu, M., Yu, X., Yu, J., 2024. Device design principles and bioelectronic applications for flexible organic electrochemical transistors. Int. J. Extrem. Manuf. 6 (1), 012005.

Garreau, S., Duvail, J.L., Louarn, G., 2001. Spectroelectrochemical studies of poly(3,4-ethylenedioxythiophene) in aqueous medium. Synth. Met. 125 (3), 325–329.

Ghittorelli, M., Lingstedt, L., Romele, P., Crăciun, N.I., Kovács-Vajna, Z.M., Blom, P.W. M., Torricelli, F., 2018. High-sensitivity ion detection at low voltages with current-driven organic electrochemical transistors. Nat. Commun. 9 (1), 1441.

Govindaraj, M., Srivastava, A., Muthukumaran, M.K., Tsai, P.-C., Lin, Y.-C., Raja, B.K., Rajendran, J., Ponnusamy, V.K., Arockia Selvi, J., 2023. Current advancements and prospects of enzymatic and non-enzymatic electrochemical glucose sensors. Int. J. Biol. Macromol. 253, 126680.

Granger, D., Marsolais, M., Burry, J., Laprade, R., 2003. Na+/H+ exchangers in the human eccrine sweat duct. Am. J. Physiol. Cell Physiol. 285 (5), C1047–C1058.

Han, J., Li, M., Li, H., Li, C., Ye, J., Yang, B., 2020. Pt-Poly(L-Lactic acid) microelectrode-based microsensor for in situ glucose detection in sweat. Biosens. Bioelectron. 170, 112675.

Handbook of Nanobioelectrochemistry, Application in Devices and Biomolecular Sensing, 2023.

Hangarter, C.M., Bangar, M., Mulchandani, A., Myung, N.V., 2010. Conducting polymer nanowires for chemiresistive and FET-Based bio/chemical sensors. J. Mater. Chem. 20 (16), 3131–3140.

Hassan, M.H., Vyas, C., Grieve, B., Bartolo, P., 2021. Recent advances in enzymatic and non-enzymatic electrochemical glucose sensing. Sensors. 21, 4672.

Hoa, L.T., Sun, K.G., Hur, S.H., 2015. Highly sensitive non-enzymatic glucose sensor based on Pt nanoparticle decorated graphene oxide hydrogel. Sensor. Actuator. B Chem. 210, 618–623.

Jeong, S., Park, S.-H., Lee, S., Cho, H., Lee, K.-y., Ju, B.K., Lee, Y.J., Lee, S.H., 2025. Electrochemical biosensor based on gold nanoparticles/laser induced graphene for diagnosis of Parkinson's disease by detecting phosphorylated α-synuclein in human blood. Chemical Engineering Journal 509, 161329.

Kaisti, M., 2017. Detection principles of biological and chemical FET sensors. Biosens. Bioelectron. 98, 437–448.

Karyakin, A.A., Puganova, E.A., Bolshakov, I.A., Karyakina, E.E., 2007. Electrochemical sensor with record performance characteristics. Angew. Chem. Int. Ed. 46 (40), 7678–7680.

Kergoat, L., Piro, B., Berggren, M., Horowitz, G., Pham, M.-C., 2012. Advances in organic transistor-based biosensors: from organic electrochemical transistors to electrolyte-gated organic field-effect transistors. Anal. Bioanal. Chem. 402 (5), 1813–1826.

Kim, S.-K., Lee, G.-H., Jeon, C., Han, H.H., Kim, S.-J., Mok, J.W., Joo, C.-K., Shin, S., Sim, J.-Y., Myung, D., Bao, Z., Hahn, S.K., 2022. Bimetallic nanocatalysts immobilized in nanoporous hydrogels for long-term robust continuous glucose monitoring of smart contact lens. Adv. Mater. 34 (18), 2110536.

Kumar, A., Purohit, B., Mahato, K., Chandra, P., 2019. Advance engineered nanomaterials in point-of-care immunosensing for biomedical diagnostics. In: Ahmed, M.U., Zourob, M., Tamiya, E. (Eds.), Immunosensors. The Royal Society of Chemistry, 0.

Lee, W.-C., Kim, K.-B., Gurudatt, N.G., Hussain, K.K., Choi, C.S., Park, D.-S., Shim, Y.-B., 2019. Comparison of enzymatic and non-enzymatic glucose sensors based on hierarchical Au-Ni alloy with conductive polymer. Biosens. Bioelectron. 130, 48–54.

Lee, I., Park, S., Lee, Y.S., Kim, Y., Kang, M.H., Yun, C., 2023. Gradual morphological change in PEDOT:PSS thin films immersed in an aqueous solution. Langmuir 39 (4), 1600–1610.

Liang, Y., Offenhäusser, A., Ingebrandt, S., Mayer, D., 2021. PEDOT:PSS-based bioelectronic devices for recording and modulation of electrophysiological and biochemical cell signals. Adv. Healthcare Mater. 10 (11), 2100061.

Liang, X., Zhang, S., Meng, S., Tan, R., Zhang, K., Hu, J., 2024. A non-enzymatic flexible and wearable sensor based on thermal transfer printing technology for continuous glucose detection in sweat. Microchem. J. 207, 111690.

Lorestani, F., Zhang, X., Abdullah, A.M., Xin, X., Liu, Y., Rahman, M.M., Biswas, M.A.S., Li, B., Dutta, A., Niu, Z., Das, S., Barai, S., Wang, K., Cheng, H., 2023. A highly sensitive and long-term stable wearable patch for continuous analysis of biomarkers in sweat. Adv. Funct. Mater. 33 (52), 2306117.

Madhu, R., Veeramani, V., Chen, S.-M., Manikandan, A., Lo, A.-Y., Chueh, Y.-L., 2015. Honeycomb-like porous carbon–cobalt oxide nanocomposite for high-performance enzymeless glucose sensor and supercapacitor applications. ACS Appl. Mater. Interfaces 7 (29), 15812–15820.

Mahapatra, S., Kumari, R., Chandra, P., 2024. Fabrication of a laser-directed electrochemical paper analytical device and its deployment for multi-functional electrochemical sensing. Chemical Engineering Journal 486, 150232.

Malik, S., Khadgawat, R., Anand, S., Gupta, S., 2016. Non-invasive detection of fasting blood glucose level via electrochemical measurement of saliva. SpringerPlus 5 (1), 701.

Mochizuki, Y., Horii, T., Okuzaki, H., 2012. Effect of pH on structure and conductivity of PEDOT/PSS. Trans. Mater. Res. Soc. Japn. 37 (2), 307–310.

Nakatsuka, N., Yang, K.-A., Abendroth, J.M., Cheung, K.M., Xu, X., Yang, H., Zhao, C., Zhu, B., Rim, Y.S., Yang, Y., Weiss, P.S., Stojanović, M.N., Andrews, A.M., 2018. Aptamer–field-effect transistors overcome debye length limitations for small-molecule sensing. Science 362 (6412), 319–324.

Niu, X., Lan, M., Zhao, H., Chen, C., 2013. Highly sensitive and selective nonenzymatic detection of glucose using three-dimensional porous nickel nanostructures. Anal. Chem. 85 (7), 3561–3569.

Okuda-Shimazaki, J., Yoshida, H., Sode, K., 2020. FAD dependent glucose dehydrogenases – discovery and engineering of representative glucose sensing enzymes. Bioelectrochemistry 132, 107414.

Onisuru, O.R., Oseghale, C.O., Meijboom, R., 2020. In situ replacement of Cu-DEN: an approach for preparing a more noble metal nanocatalyst for catalytic use. New J. Chem. (1987) 44 (46), 20322–20333.

Pappa, A.M., Ohayon, D., Giovannitti, A., Maria, I.P., Savva, A., Uguz, I., Rivnay, J., McCulloch, I., Owens, R.M., Inal, S., Direct metabolite detection with an n-type accumulation mode organic electrochemical transistor. Sci. Adv. 4(6), eaat0911.

Park, S., Boo, H., Chung, T.D., 2006. Electrochemical non-enzymatic glucose sensors. Anal. Chim. Acta 556 (1), 46–57.

Purohit, B., Kumar, A., Mahato, K., Chandra, P., 2020. Novel sensing assembly comprising engineered gold dendrites and MWCNT-AuNPs nanohybrid for acetaminophen detection in human urine. Electroanalysis 32 (3), 561–570.

Reddy, V., Agarwal, B., Ye, Z., Zhang, C., Roy, K., Chinnappan, A., Narayan, R., Ramakrishna, S., Ghosh, R., 2022. Recent advancement in biofluid-based glucose sensors using invasive, minimally invasive, and non-invasive technologies: a review. Nanomaterials (Basel) 12, 1082.

Rodríguez-González, P., Marchante-Gayón, J.M., García Alonso, J.I., Sanz-Medel, A., 2005. Isotope dilution analysis for elemental speciation: a tutorial review. Spectrochim. Acta B Atom Spectrosc. 60 (2), 151–207.

Rollo, S., Rani, D., Olthuis, W., Pascual García, C., 2020. High performance Fin-FET electrochemical sensor with high-k dielectric materials. Sensor. Actuator. B Chem. 303, 127215.
Sempionatto, J.R., Lin, M., Yin, L., De la paz, E., Pei, K., Sonsa-ard, T., de Loyola Silva, A. N., Khorshed, A.A., Zhang, F., Tostado, N., Xu, S., Wang, J., 2021. An epidermal patch for the simultaneous monitoring of haemodynamic and metabolic biomarkers. Nat. Biomed. Eng. 5 (7), 737–748.
Sheldon, R.A., van Pelt, S., 2013. Enzyme immobilisation in biocatalysis: why, what and how. Chem. Soc. Rev. 42 (15), 6223–6235.
Siddiqui, S., Arumugam, P.U., Chen, H., Li, J., Meyyappan, M., 2010. Characterization of carbon nanofiber electrode arrays using electrochemical impedance spectroscopy: effect of scaling Down electrode size. ACS Nano 4 (2), 955–961.
Sophocleous, M., Contat-Rodrigo, L., García-Breijo, E., Georgiou, J., 2021. Organic electrochemical transistors as an emerging platform for bio-sensing applications: a review. IEEE Sens. J. 21 (4), 3977–4006.
Søpstad, S., Johannessen, E.A., Seland, F., Imenes, K., 2018. Long-term stability of screen-printed pseudo-reference electrodes for electrochemical biosensors. Electrochim. Acta 287, 29–36.
Tang, H., Yan, F., Lin, P., Xu, J., Chan, H.L.W., 2011. Highly sensitive glucose biosensors based on organic electrochemical transistors using platinum gate electrodes modified with enzyme and nanomaterials. Adv. Funct. Mater. 21 (12), 2264–2272.
Tehrani, F., Bavarian, B., 2016. Facile and scalable disposable sensor based on laser engraved graphene for electrochemical detection of glucose. Sci. Rep. 6 (1), 27975.
Thanh, T.D., Balamurugan, J., Lee, S.H., Kim, N.H., Lee, J.H., 2016a. Effective seed-assisted synthesis of gold nanoparticles anchored nitrogen-doped graphene for electrochemical detection of glucose and dopamine. Biosens. Bioelectron. 81, 259–267.
Thanh, T.D., Balamurugan, J., Hwang, J.Y., Kim, N.H., Lee, J.H., 2016b. In situ synthesis of graphene-encapsulated gold nanoparticle hybrid electrodes for non-enzymatic glucose sensing. Carbon 98, 90–98.
Torricelli, F., Adrahtas, D.Z., Bao, Z., Berggren, M., Biscarini, F., Bonfiglio, A., Bortolotti, C.A., Frisbie, C.D., Macchia, E., Malliaras, G.G., McCulloch, I., Moser, M., Nguyen, T.-Q., Owens, R.M., Salleo, A., Spanu, A., Torsi, L., 2021. Electrolyte-gated transistors for enhanced performance bioelectronics. Nature Rev. Methods Prim. 1 (1), 66.
Valdes, T.I., Moussy, F., 2000. In vitro and in vivo degradation of glucose oxidase enzyme used for an implantable glucose biosensor. Diabetes Technol. Therapeut. 2 (3), 367–376.
Volmer, D.A., Mendes, L.R., Stokes, C.S., 2015. Analysis of vitamin D metabolic markers by mass spectrometry: current techniques, limitations of the "gold standard" method, and anticipated future directions. Mass Spectrom. Rev. 34 (1), 2–23.
Wang, B., Zhao, C., Wang, Z., Yang, K.-A., Cheng, X., Liu, W., Yu, W., Lin, S., Zhao, Y., Cheung, K.M., Lin, H., Hojaiji, H., Weiss, P.S., Stojanović, M.N., Tomiyama, A.J., Andrews, A.M., Emaminejad, S., Wearable aptamer-field-effect transistor sensing system for noninvasive cortisol monitoring. Sci. Adv. 8(1), eabk0967.
Wilson, R., Turner, A.P.F., 1992. Glucose oxidase: an ideal enzyme. Biosens. Bioelectron. 7 (3), 165–185.
Won, S.-Y., Chandra, P., Hee, T.S., Shim, Y.-B., 2013. Simultaneous detection of antibacterial sulfonamides in a microfluidic device with amperometry. Biosens. Bioelectron. 39 (1), 204–209.
Wu, W., Feng, K., Wang, Y., Wang, J., Huang, E., Li, Y., Jeong, S.Y., Woo, H.Y., Yang, K., Guo, X., 2024. Selenophene substitution enabled high-performance n-Type polymeric mixed ionic-electronic conductors for organic electrochemical transistors and glucose sensors. Adv. Mater. 36 (1), e2310503.
Xu, Q., Yin, L., Hou, C., Liu, X., Hu, X., 2012. Facile fabrication of nanoporous platinum by alloying–dealloying process and its application in glucose sensing. Sensor. Actuator. B Chem. 173, 716–723.
Xu, M., Song, Y., Ye, Y., Gong, C., Shen, Y., Wang, L., Wang, L., 2017. A novel flexible electrochemical glucose sensor based on gold nanoparticles/polyaniline arrays/carbon cloth electrode. Sensor. Actuator. B Chem. 252, 1187–1193.
Xu, C., Song, Y., Sempionatto, J.R., Solomon, S.A., Yu, Y., Nyein, H.Y.Y., Tay, R.Y., Li, J., Heng, W., Min, J., Lao, A., Hsiai, T.K., Sumner, J.A., Gao, W., 2024. A physicochemical-sensing electronic skin for stress response monitoring. Nature Electronics 7 (2), 168–179.
Yang, Y.-C., Park, J., Kim, J., Choi, A., Park, C.O., 2009. The study of the voltage drift in high-temperature proton conductor-based hydrogen sensors adopting the solid reference electrode. Sensor. Actuator. B Chem. 140 (1), 273–277.
Yao, Y., Huang, W., Chen, J., Liu, X., Bai, L., Chen, W., Cheng, Y., Ping, J., Marks, T.J., Facchetti, A., 2023. Flexible and stretchable organic electrochemical transistors for physiological sensing devices. Adv. Mater. 35 (35), 2209906.
Yu, Z., Jiang, N., Kazarian, S.G., Tasoglu, S., Yetisen, A.K., 2021. Optical sensors for continuous glucose monitoring. Prog. Biomed. Eng. 3 (2), 022004.
Zahed, M.A., Barman, S.C., Das, P.S., Sharifuzzaman, M., Yoon, H.S., Yoon, S.H., Park, J. Y., 2020. Highly flexible and conductive poly (3, 4-ethylene dioxythiophene)-poly (styrene sulfonate) anchored 3-dimensional porous graphene network-based electrochemical biosensor for glucose and pH detection in human perspiration. Biosens. Bioelectron. 160, 112220.
Zhang, M., Liao, C., Yao, Y., Liu, Z., Gong, F., Yan, F., 2014a. High-performance dopamine sensors based on whole-graphene solution-gated transistors. Adv. Funct. Mater. 24 (7), 978–985.
Zhang, L., Chen, J., Wang, Y., Yu, L., Wang, J., Peng, H., Zhu, J., 2014b. Improved enzyme immobilization for enhanced bioelectrocatalytic activity of choline sensor and acetylcholine sensor. Sensor. Actuator. B Chem. 193, 904–910.
Zhang, L., Wang, G., Wu, D., Xiong, C., Zheng, L., Ding, Y., Lu, H., Zhang, G., Qiu, L., 2018. Highly selective and sensitive sensor based on an organic electrochemical transistor for the detection of ascorbic acid. Biosens. Bioelectron. 100, 235–241.
Zhang, Y., Chen, Y., Huang, J., Liu, Y., Peng, J., Chen, S., Song, K., Ouyang, X., Cheng, H., Wang, X., 2020. Skin-interfaced microfluidic devices with one-opening chambers and hydrophobic valves for sweat collection and analysis. Lab Chip 20 (15), 2635–2645.
Zhang, T., Li, Y., Lv, X., Jiang, S., Jiang, S., Sun, Z., Zhang, M., Li, Y., 2024. Ultra-sensitive and unlabeled SERS nanosheets for specific identification of glucose in body fluids. Adv. Funct. Mater. 34 (17), 2315668.
Zhao, Y., Jin, K.-Q., Li, J.-D., Sheng, K.-K., Huang, W.-H., Liu, Y.-L., 2023. Flexible and stretchable electrochemical sensors for biological monitoring. Adv. Mater. n/a (n/a), 2305917.
Zheng, X.T., Leoi, M.W.N., Yu, Y., Tan, S.C.L., Nadzri, N., Goh, W.P., Jiang, C., Ni, X.P., Wang, P., Zhao, M., Yang, L., 2024. Co-Encapsulating enzymes and carbon dots in metal–organic frameworks for highly stable and sensitive touch-based sweat sensors. Adv. Funct. Mater. 34 (10), 2310121.
Zhu, H., Li, L., Zhou, W., Shao, Z., Chen, X., 2016. Advances in non-enzymatic glucose sensors based on metal oxides. J. Mater. Chem. B 4 (46), 7333–7349.
Zhu, J., Liu, S., Hu, Z., Zhang, X., Yi, N., Tang, K., Dexheimer, M.G., Lian, X., Wang, Q., Yang, J., Gray, J., Cheng, H., 2021a. Laser-induced graphene non-enzymatic glucose sensors for on-body measurements. Biosens. Bioelectron. 193, 113606.
Zhu, B., Yu, L., Beikzadeh, S., Zhang, S., Zhang, P., Wang, L., Travas-Sejdic, J., 2021b. Disposable and portable gold nanoparticles modified - laser-scribed graphene sensing strips for electrochemical, non-enzymatic detection of glucose. Electrochim. Acta 378, 138132.